Advancing RIS Beamforming Efficiency: Moving Beyond Diagonal Matrix Techniques

Javad Shabanpour, Xuchen Wang, Sergei Kosulnikov, Constantin Simovski

***Abstract*—Optimizing wireless propagation channels is essential for advancing future communication technologies, particularly in dynamic vehicular environments where high vehicle mobility is a challenge. This paper introduces a novel practical implementation of reconfigurable intelligent surfaces (RIS) that achieve highly efficient beamforming, significantly surpassing the limitations of the conventional diagonal phase shift approach. We expand the theoretical and optimization framework based on the discrete impedance model to accommodate practical design scenarios. We validate our approach by fabricating an RIS prototype and conducting experimental measurements using the parallel plate waveguide technique. The experimental results confirm the superior performance of our approach, demonstrating at least a 30% improvement in efficiency over diagonal matrix methods, thereby enhancing signal quality and coverage. This ensures seamless communication and ubiquitous connectivity, improving the quality of service by boosting the received signal.**

***Index Terms*—Reconfigurable Intelligent Surface (RIS), Wireless communication, Beamforming.**

I. Introduction

THE rapid advancements in wireless communication technologies have driven the development of next-generation vehicular communication systems, which are essential for realizing intelligent transportation systems (ITS) and autonomous driving [1], [2]. A primary challenge in vehicular communication is maintaining robust and reliable connectivity in *dynamic environments*. High-speed vehicle movement causes frequent changes in communication channel characteristics, leading to issues such as signal blockage, multipath fading, and Doppler shifts [3].

In technical terms, areas with large structures like skyscrapers or trucks often experience significant disruptions in wireless connections between ground-based infrastructure and vehicles. This results in a decline in service quality, sometimes for prolonged duration. Additionally, some locations where obstacles greatly obstruct the Line of Sight (LoS) remain consistently out of coverage (dark zones). Extending wireless coverage to these undeserved leads to a substantial increase in costs [4]. Meanwhile, the reconfigurable intelligent surface (RIS) is a flat panel composed of active or passive elements that can modify the communication environment, allowing user equipment (UE) to receive signals in so-called non-line-of-sight directions. The key objectives of RISs are to boost wireless link performance and efficiency, improve signal quality, expand coverage range, and reduce the need for a high-power transmission [5].

The diagonal matrix technique is widely utilized for RIS design in current RIS-based wireless communication which is represnted as:

$$\mathbf{\Theta} = \text{diag}\left(\beta_1 e^{j\theta_1}, \beta_2 e^{j\theta_2}, \ldots, \beta_N e^{j\theta_N}\right)$$

, where β_i is the reflection amplitude and θ_i is the phase shift introduced by the i-th RIS element [6], [7]. The locally periodic approximation is taken into consideration to ensure that each unit cell scatters the incoming wave without impacting the adjacent unit cells. Fig.1 of [8] illustrates this technique. By varying the local reflection phases gradually and considering the free-space channel between the transmitter and receiver, the RIS can deflect the incoming energy in a specific direction. The angle of this anomalous reflection is determined by the incident angle and the slope of the local reflection phase, via the so-called generalized law of reflection [9]. A detailed discussion about the approximation of reflection locality which is necessary to utilize the local periodicity assumption can be found in [10].

Even with this rough approximation, the efficiency of anomalous reflectors designed using this method decreases drastically as the deflection angle (the difference between the incidence and reflection angles) increases. However, this phenomenon is problematic because it can significantly reduce the quality of service (QoS) for passing vehicles, disrupting real-time connectivity. Our investigations in the paper demonstrates that the efficiency of the RIS using the diagonal matrix approach is at least 30% lower than that of our proposed method, representing a significant difference. Consequently, the received signal strength falls within the detectable range of the receivers. This disruption can lead to interruptions in seamless connectivity, which is especially difficult for applications that depend on continuous and stable connections.

Theoretically speaking, [11] revealed that the reason for this inherent limitation of locally passive surfaces is the impedance mismatch between impinging and desired wavefronts. Therefore, perfect anomalous reflection goes beyond the scope of physical optics, and requires to take into account the evanescent modes excited on the reflecting surface [12]. By addressing the impedance mismatch issue, it may be possible to significantly improve the efficiency of reflectors, even at

This project has received funding from the European Union's Horizon 2020 research and innovation programme under the Marie SkŁodowska-Curie grant agreement No 956256. Also, authors have no conflict of interest. (Corresponding author: Javad Shabanpour.)

J. Shabanpour, S. Kosulnikov, and C. Simovski are with the Department of Electronics and Nanoengineering, Aalto University, 00079 Aalto, Finland (e-mail: mohammadjavad.shabanpoursheshpoli@aalto.fi; sergei.2.kosulnikov@aalto.fi; konstantin.simovski@aalto.fi). X. Wang is with the Institute of Nanotechnology, Karlsruhe Institute of Technology, 76131 Karlsruhe, Germany (e-mail: xuchen.wang@kit.edu)

larger deviation angles. Up to now, advanced techniques have been suggested for achieving perfect anomalous reflection using so-called non-local metasurfaces [13], [14] and so-called metagratings – sparse arrays of subwavelength reflecting elements [15], [16]. In [17], a general method for synthesizing metasurfaces (planar arrays of subwavelength unit cells) for perfect reflection and refraction was proposed using an equivalent impedance matrix model. Additionally, [18] and [19] introduced approaches for achieving perfect anomalous reflection, demonstrating that a specific and strongly non-local response of a metasurface (MS) to the incident wave, rather than a local response (diagonal matrix), is required. While these non-local approaches are theoretically sound and physically consistent, most of them are impractical for real-world applications.

In [20], the authors introduced a design approach for highly efficient anomalous reflection using a nonuniform impedance sheet on a metal-backed dielectric substrate. However, the static nature of the RIS limits its adaptability to rapidly changing environments. Dynamic reconfigurability is crucial for vehicle-to-everything (V2X) communication, where maintaining seamless connectivity is essential for safety, traffic management, and autonomous driving. Real-time adjustments in RIS can optimize signal paths and enhance link quality, addressing the limitations of static designs.

To address these challenges, we introduce a practical approach for designing realistic RIS utilizing the surface impedance method by expanding our previously reported technique [20] . This method not only achieves effective dynamic beamforming but also addresses the inefficiencies of the traditional diagonal matrix model, which often suffers from low reradiation efficiency and generates multiple parasitic modes. Our contributions are summarized as follows:

- First, we briefly outline the preliminaries for obtaining scattered waves from the RIS using known surface impedance. Next, we introduce our optimization framework in Matlab to inversely design the RIS and derive the required surface/sheet impedance for achieving our predefined goal—maximizing the received signal strenght by the user equipment (P_1= P_2 as depicted in Fig.1(a)). P_1 and P_2 denote the peak power of the incident and scattered wave.
- Using the Matlab-optimized surface/sheet impedance values, we design the unitcell covers the necessary impedance range in the FR3 band (carrier frequency of 8 GHz). By adjusting the capacitances of the varactor diodes, the RIS can achieve the desired impedances within this range.
- We verify our designed RIS performance through full-wave numerical simulations using CST Microwave Studio. We compare the efficiency of our surface impedance approach with the diagonal matrix method, offering at least a 30% improvement. This improvement is especially significant for larger deflection angles, where the diagonal matrix method fails to scatter the waves effectively.
- Additionally, we validate our approach by fabricating a RIS prototype and conducting experimental measurements using the parallel plate waveguide technique. We also propose our novel biasing approach for testing reconfigurable surfaces inside the parallel-plate waveguide. This method offers significant advantages in terms of cost-effectiveness, making it highly beneficial for practical application. The measurements aligned with our theoretical predictions. By varying the varactor bias voltage with a DC supply network, we compare the measurement results of our method with the diagonal matrix technique demonstrating the superior performance of our approach.

Note that the concept of RIS with beyond-diagonal matrix techniques (BD-RIS) has been extensively studied in recent literature [21]–[24]. BD-RIS design and modeling, such as the scattering parameter network analysis by Shen et al. [21], which provides a foundational approach for RIS configurations that go beyond conventional diagonal structures. Also the work by Li et al. [22], explores fully connected and group-connected architectures for BD-RIS, offering a broader context for the flexibility of BD-RIS in diverse communication scenarios. But, our approach diverges from these studies by focusing on a discrete impedance model designed for high-efficiency beamforming, specifically tailored to mitigate issues like mirror reflections while enhancing adaptability. Unlike the fully connected architectures in BD-RIS studies, our model emphasizes on optimizaing into the supercell scale to directly mitigate the undesired reflection while considering the internal coupling between the unitcells.

While RIS-assisted systems show great promise, their practical deployment is often hindered by imperfect channel state information (CSI), which can arise due to hardware impairments, estimation errors, or feedback delays. Several studies have analyzed these limitations. For instance, [25] evaluates the ergodic spectral efficiency of omni-surface aided systems under both hardware impairments and imperfect CSI. Similarly, [26] explores the achievable rate in STAR-RIS-aided NOMA uplinks, highlighting the compound effect of CSI errors and hardware distortion. The work in [27] focuses on active RIS systems and shows how imperfect CSI and phase noise degrade performance. These studies emphasize the importance of robust design strategies to mitigate such real-world impairments. Although our current work assumes perfect CSI to focus on demonstrating the fundamental performance gain of discrete impedance modeling, future extensions can integrate CSI uncertainty into the optimization framework.

Although RIS technology offers promising advantages, several challenges hinder its practical deployment. These include:

1- Modeling Inaccuracy: Most existing RIS models oversimplify real-world electromagnetic interactions, leading to a gap between simulated and actual performance.

2- Fabrication Costs: High-frequency, low-loss tunable components like varactors remain expensive, making large-scale, cost-effective production difficult.

3- Deployment Logistics: Effective RIS placement often requires access to building facades or windows, creating logistical and regulatory hurdles, especially in urban areas.

4- OFDM Compatibility: RIS struggles to maintain consistent performance across the fast frequency variations in OFDM systems, limiting its integration with current 4G/5G technologies.

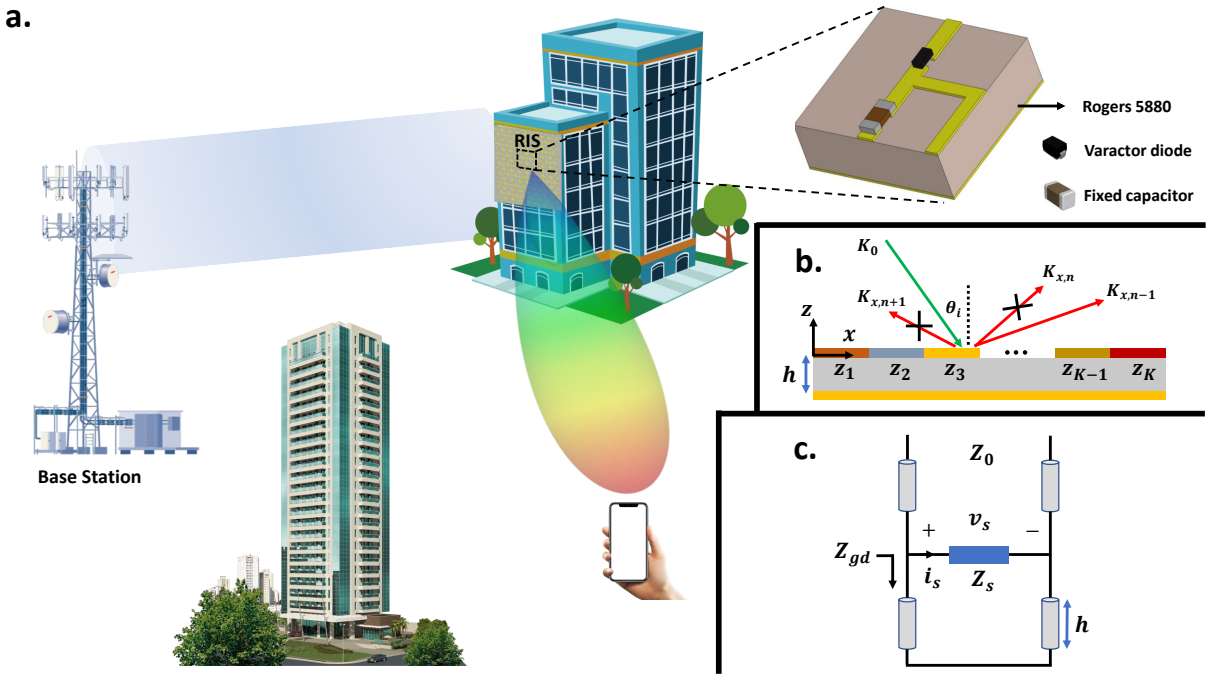

Fig. 1. a) Application scenario of a highly efficient RIS in dynamic seamless wireless communication where a single automobile UE can receive all the incident energy from the base station in downlink. There is the same situation in uplink wireless communication. On the inset a unitcell of the loaded microstrip wire is shown. b) Side view of a RIS composed of discrete impedance strips on a grounded substrate. The aim of the optimization is to suppress all the Floquet-Bloch harmonics except the desired one (here n =+1). c) Equivalent circuit of the proposed RIS.

Despite these challenges, RIS continues to attract strong interest from academia and industry. While not yet standardized in current cellular networks, RIS is widely considered a foundational technology for 6G. Unlike traditional systems that adapt antennas to the environment, RIS redefines the environment itself—making it programmable and intelligent.

Recent advancements in RIS design have focused on enhancing reconfigurability and efficiency through higher control granularity and vertical integration. For instance, [28] presents a 2-bit RIS prototype capable of rapid space-time wavefront manipulation, demonstrating the feasibility of hardware-accelerated RIS adaptation. Meanwhile, multilayer or stacked intelligent metasurfaces have emerged as a promising path for implementing beyond-diagonal architectures, with demonstrated benefits in holographic MIMO and 6G applications [29], [30]. These approaches complement our method, which targets efficient and scalable beamforming using discrete impedance control optimized at the supercell level.

The model we propose in this work fundamentally differs from the approach in [21], which utilizes a scattering parameter network analysis to model fully connected and group connected RIS architectures. The fully connected and group-connected impedance networks enable adjustment of both the phase and amplitude of the impinging waves, achieving notable power gains in scenarios like Rayleigh fading. In contrast, our discrete impedance model is built upon surface impedance control rather than scattering parameters. This independence from inter-element coupling allows us to directly optimize each unit cell impedance without requiring full matrix interactions, enabling faster adjustments and reduced complexity in tuning phases and amplitudes at each element. Also, in [21], the fully and group-connected models require complex impedance networks with substantial inter-element coordination. Our model's design focuses on tuning discrete impedance values individually, simplifying hardware requirements and enhancing feasibility for real-world, large-area deployments.

II. Theory

A. From surface impedance to Scattered Modes

In our RIS, each unit cell shares the same shape while exhibiting varying load impedance values, as it is clear from the inset of Fig.1(a). A single supercell of our periodic RIS comprises K unit cells – the side view of the supercell is schematically shown in Fig.1(b). The prerequisite of the employed method is modal transmission line model illustrated by Fig.1(c), where the grounded dielectric substrate is presented as a shorted transmission line of length h equal to the substrate thickness. Its input impedance Z_{gd} for important modes is inductive, whereas the top grid has the capacitive sheet impedance Z_s shunting Z_{gd}. Tangential components of the magnetic and electric fields (z = 0) are I_s and V_s, respectively. By knowing the surface impedance for given incidence angle, it is possible to uniquely determine the amplitudes and phases of all scattered Floquet harmonics through the mode-matching technique ([31], Sec. 6.2) at the MS plane ($z = 0$). Here, we describe the details of the mathematical model.

The sheet impedance $Z_s(x)$ or admittance $Y_s(x)$ of a metasurface (MS) with period D is a periodical function that

can be represented by the Fourier series:

$$Z_s(x) = \sum_{m=-\infty}^{+\infty} a_m e^{-jm\beta_M x} \tag{1}$$

$$Y_s(x) = \sum_{m=-\infty}^{+\infty} b_m e^{-jm\beta_M x} \tag{2}$$

in which $\beta_M = 2\pi/D$ is the spatial modulation frequency of the surface impedance, and a_m, b_m are the Fourier coefficients of the impedance and admittance functions, respectively. When a periodic surface is illuminated by a plane wave at an incident angle θi, discrete sets of Floquet harmonics are scattered, comprising both propagating and evanescent waves. The tangential wave number of these scattered Floquet modes is expressed as $k_{xn} = k_0 \sin\theta_i + n\beta_M$, where k_0 is the wavenumber in free space and is equal to $k_0 = \omega_0\sqrt{\varepsilon_0\mu_0}$, with ω_0 representing the angular frequency of the incoming plane wave, and n is the number of Floquet harmonics. The propagating modes with reflection angle θr in the far-field zone are those modes that satisfy $|k_{xn}| < k_0$. Thus, we can express the reflection angle of the n-th propagating mode as:

$$\sin\theta_{r,n} = \sin\theta_i - \frac{n\lambda}{D} \tag{3}$$

where λ is the working wavelength. Conversely, when the magnitude of k_{xn} exceeds k_0, a portion of the energy from the incident wave is converted into evanescent modes, which are waves that exponentially decay along the surface.

As the periodically modulated MS generates an infinite number of spatial harmonics, it becomes feasible to express the corresponding voltage V_s and current I_s as infinite series of modal voltages and currents:

$$I_s(x) = \sum_{n=-\infty}^{+\infty} i_s^n e^{-jk_{xn}x} \tag{4}$$

$$V_s(x) = \sum_{n=-\infty}^{+\infty} v_s^n e^{-jk_{xn}x} \tag{5}$$

For the discrete impedance sheet modeled as shunt impedance, the current and voltage should adhere to Ohm's law. By substituting Eq. 4 and Eq. 5 into Ohm's law equation ($V_s(x) = Z_s(x).I_s(x)$), we can derive:

$$\sum_{n=-\infty}^{+\infty} v_s^n e^{-jk_{xn}x} = \sum_{m=-\infty}^{+\infty}\sum_{n=-\infty}^{+\infty} a_m i_s^n e^{-jk_{x,n+m}x} \tag{6}$$

We can simplify both sides of the equation by applying a transformation of n to $n-m$ on the right-hand side, resulting in the use of a common basis function. This can be expressed as:

$$v_s^n = \sum_{m=-\infty}^{+\infty} a_m i_s^{n-m} \tag{7}$$

The implication of Eq. 7 is that the generation of any given voltage harmonic is dependent on all current harmonics which displays mode coupling. By considering a finite number of Floquet harmonics from $-N$ to N, the matrix form of Eq. 7 can be expressed as:

$$\begin{pmatrix} v_s^{-N} \\ v_s^{1-N} \\ \vdots \\ v_s^{+N} \end{pmatrix} = \begin{pmatrix} a_0 & a_{-1} & \cdots & a_{-2N} \\ a_1 & a_0 & \cdots & a_{1-2N} \\ \vdots & \vdots & \ddots & \vdots \\ a_{2N} & a_{2N-1} & \cdots & a_0 \end{pmatrix} \begin{pmatrix} i_s^{-N} \\ i_s^{1-N} \\ \vdots \\ i_s^{+N} \end{pmatrix} \tag{8}$$

In Eq. 8, we observe that the current and voltage vectors have a direct correlation with a Toeplitz impedance matrix $\mathbf{Z_s}'$. This matrix is constructed using the Fourier coefficients of discretized sheet impedance $Z_s(x)$, which are represented as $\mathbf{Z_s}'(u,v) = a_{u-v}$. A useful aspect of Toeplitz matrices is their ability to be diagonally transformed using the fast Fourier transformation algorithm, that makes their computation highly efficient.

In order to determine the overall surface impedance of the MS corresponding to the given n-th mode, it is necessary to compute the surface impedance of the grounded substrate. As the substrate is spatially homogeneous, the impedance matrix $\mathbf{Z_{gd}}$ contains only diagonal elements, which are of $2N+1$ dimensions. The n-th diagonal component of this matrix for the n-th Flouqet harmonic for both orthogonal polarizations can be expressed as:

$$\mathbf{Z}_{gd}^{TE}(n,n) = \frac{k_{zn}^d}{\mu_0\omega_0 \tanh(jk_{zn}^d h)} \tag{9}$$

$$\mathbf{Z}_{gd}^{TM}(n,n) = \frac{\omega_0\varepsilon_0\varepsilon_d}{k_{zn}^d \tanh(jk_{zn}^d h)} \tag{10}$$

in which $k_{zn}^d = \sqrt{\omega_0^2\varepsilon_0\mu_0\varepsilon_d - k_{xn}^2}$ is the normal component of the wave vector in the dielectric slab.

Now, all the matrices are available for calculating the modal surface impedance of the MS, $\mathbf{Z_{tot}}$ which can be defined as a parallel connection of the matrix of discretized sheet impedance ($\mathbf{Z_s}$) and the matrix of the uniform impedance of the grounded dielectric substrate ($\mathbf{Z_{gd}}$) i.e. $\mathbf{Z_{tot}} = \mathbf{Z_s}||\mathbf{Z_{gd}}$. The following step involves determining the phase and amplitude of all the scattered modes for a given incident angle, which can be accomplished by utilizing Eq. 11 and Eq. 12.

$$\mathbf{\Gamma}_{TM} = \frac{\mathbf{Z}_0 - \mathbf{Z}_{tot}}{\mathbf{Z}_0 + \mathbf{Z}_{tot}} \tag{11}$$

$$\mathbf{\Gamma}_{TE} = \frac{\mathbf{Y}_0 - \mathbf{Y}_{tot}}{\mathbf{Y}_0 + \mathbf{Y}_{tot}} \tag{12}$$

where $\mathbf{Z}_0$ is the diagonal matrix of free space wave impedance corresponding to the given mode. Finally, the tangential component of the reflected electric and magnetic fields can be calculated as $\mathbf{E_r} = \mathbf{\Gamma}_{TE} \cdot \mathbf{E_i}$ for TE, and $\mathbf{H_r} = \mathbf{\Gamma}_{TM} \cdot \mathbf{H_i}$ for TM polarized waves respectively where $\mathbf{E_i}$ and $\mathbf{H_i}$ represent the incident electric and magnetic field vector.

B. Inverse Optimization of discrete sheet impedance

In Section II-A, we reviewed the computation of scattered harmonics for discrete impedance sheets and incident waves. However, designing a metasurface involves solving an *inverse problem*, where the goal is to determine the appropriate sheet

impedance by specifying the incident and reflected electric fields. Our approach to this inverse problem consists of three steps, detailed as follows.

*1) **Determining the supercell period**:* Using diffraction grating theory (Eq. 3), we determine the period of one supercell based on the incident and desired anomalous reflection angles. The supercell is then divided into K unit cells, where $Z_{1...K}$ represents the discrete sheet impedance for the unit cells.

*2) **Specifying Incident and Reflected Fields**:* Since in this study we consider an incident wave whose electric field is parallel to the wires, for forming the incident electric field vector, only the 0-order element of the 1D matrix is unity meaning that the RIS is illuminated by the mode n=0, e.g. $\mathbf{E}_i = [0, ...0, 1, 0, ...0]^T$. In an important application, on which we concentrate in this paper, the RIS should generate one single anomalous reflection for a single UE at the specific time slot. In this case, the ideal RIS fully deflects the incident power to the harmonic n=+1. A reconfigurable surface should switch this single reflected wave with optimal efficiency towards different automobile UE in real-time. Having in mind this application, the reflected electric field vector can be expressed as $\mathbf{E_r} = [0, ...0, 0, A_{\text{goal}}, ...0]^T$. Based on [17], for an ideal MS, $A_{\text{goal}} = \sqrt{\cos\theta_i / \cos\theta_r}$.

*3) **Mathematical optimization**:* The overall scheme of the optimization is as follows: we define some initial values for discrete sheet impedance (${Z^i}_{1...K}$). Based on Eq. 3, we set the RIS period (length of the supercell) based on our desired reflection angle. K would be the number of unitcells in each period. In each trial of the optimization, Matlab assumes an explicit array $Z_{1...K}$ and then calculates the amplitude of the reflected harmonic A_{cal}. By defining the cost function as $F(Z_{1...K}) = |A_{\text{cal}} - A_{\text{goal}}|$ and employing the MultiStart and Fmincon optimization algorithms, Matlab searches the proper matrix $Z_{1...K}$ that minimizes the cost function i.e. maximal reflected power in the prescribed direction w.r.t the incident power. The general framework of the optimization provided in **Appendix. A**.

It is worth mentioning that the similar technique is highly versatile and can be applied not only to a reflective but also to a transmitting RIS, utilizing the local transfer (ABCD) matrix instead of the local surface impedance. Here the paper [16] is helpful because it outlines a comprehensive method for the multilayer cascade of modulated impedance sheets, obtained by combining the transfer matrices of individual layers. In principle, with the modification of the objective function, one can achieve an multiple-beam RIS with customized power ratios.

III. Investigation and Numerical Validation

A. Preliminary remarks

The aim of this paper is to develop a practical RIS that allows a single automobile UE to efficiently receive the maximum amount of transmitted signal from the base station, during each time slot. This solution addresses the highly dynamic nature of vehicular networks. The switching time for perfect anomalous reflection between different automobile UEs, especially given the high mobility of vehicles, is crucial. Our practical RIS is designed to effectively manage this rapid switching, ensuring optimal performance in fast-moving vehicular environments.

Our target use case focuses on using RIS to improve service coverage at FR3 frequencies. The 3rd Generation Partnership Project (3GPP) release 16 initiated the exploration of New Radio (NR) in the 7–24 GHz range [32]. To demonstrate that our RIS achieves higher efficiency than a conventionally engineered diagonal RIS, we consider the challenging case of a normally incident wave and large deflection – when the reflection angle is in the range $60^\circ - 90^\circ$. In this case, the reflection locality approximation is not adequate and the conventional phase-gradient algorithm leads to significant parasitic scattering. Meanwhile for modest deflection angles $30^\circ - 60^\circ$, the assumption of local reflection is often valid, and it is possible to engineer the linear variation of the local reflection phase along the trace of the incidence plane using the conventional method. In our case, it simply implies the different distribution of biasing voltages compared to that obtained using our method. As to the deflection angles below 30°, here we may utilize the slowly-varying phase method, also based on the the assumption of the reflection locality. The biasing scheme for this case was suggested in [11], [33], where the very high efficiency of anomalous reflection (defined as the ratio $|A_{\text{cal}}/A_{\text{goal}}|^2$) was obtained for a MS of parallel periodically loaded wires.

Thus, we divide the angular range of our RIS into three regions and use different schemes of biasing for them. However, in the end, we show the advantage of our method compared to the diagonal phase shift particularly for the range $60^\circ - 90^\circ$.

B. Deflection angles $60^\circ - 90^\circ$

The operation frequency is 8 GHz and the width of each unit cell is P = 4.8 mm. Based on Eq. 3 we should have the anomalous reflection with the reflection angle θ_r which is equal to the deflection angle since $\theta_{inc} = 0$. The period of our RIS should be equal $D = \lambda / \sin\theta_r$. By setting e.g. $\theta_r = 77^\circ$ we obtain $D = 8P$, i.e. K=8. We select Rogers RT5880 as a substrate. It has the relative permittivity 2.2, thickness $h = 1.575$ mm, and loss tangent 0.0002. In order to simplify the practical implementation of the sheet impedance, we have employed an optimization technique that ensures the sheet reactance $Z_{1...K}$ falls within the range of $[-300j, -50j]$. Without this optimization constraint, it would be challenging to find a suitable varactor diode capable of meeting the necessary variations of capacitance.

For each scenario, our numerical optimization generates a set of discrete sheet impedances which correspond to local surface impedances of the unit cells. In Fig.2(a), we present the Matlab results of the optimized scattered harmonic amplitudes for an infinite periodic structure with K=8 ($\theta r = 77^\circ$). The discrete sheet impedance values are as follows:

$$Z_{1\text{–}8} = [-103j, -82j, -80j, -123j, -185j, \\ -111j, -146j, -91j]. \tag{13}$$

The comparison of non-normalized scattering amplitudes calculated for the operational frequency in Fig.2(a) shows that

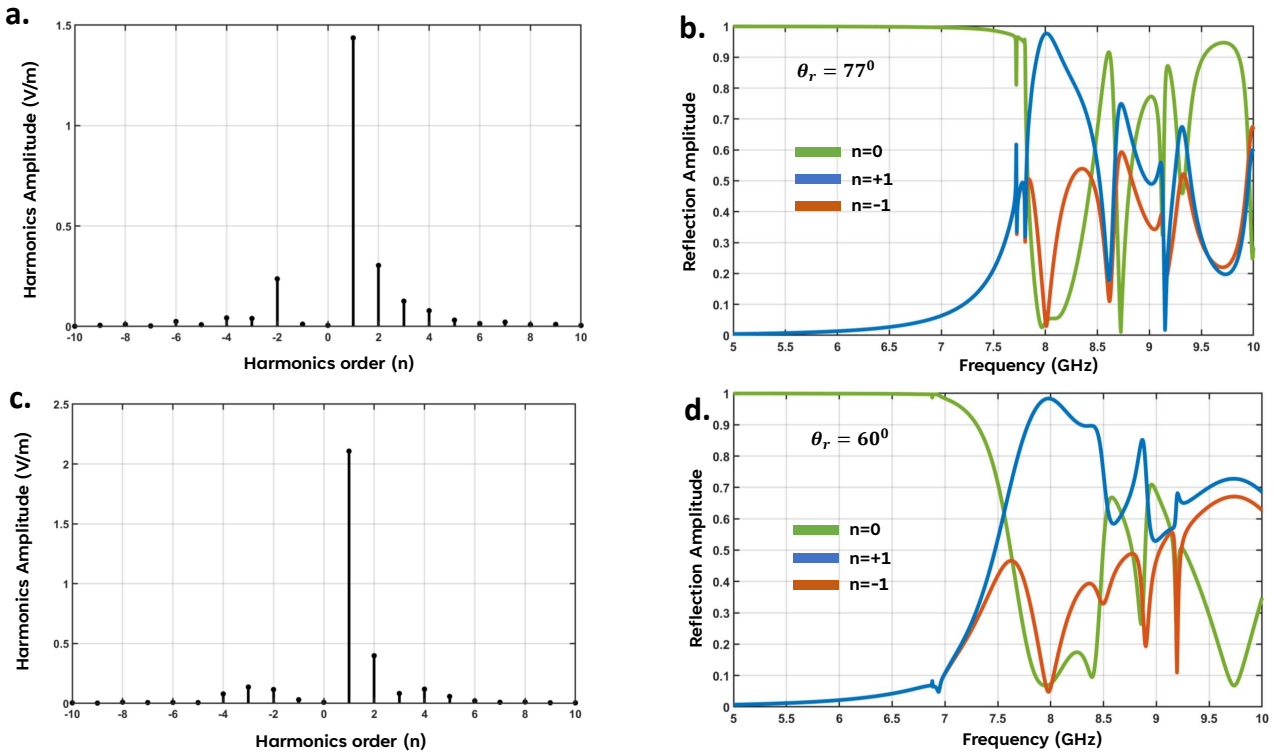

Fig. 2. Amplitudes of all scattered spatial harmonics for the RIS with optimized discrete impedance sheet for a) K=8 ($\theta_r = 77°$) ,and c) K=9 ($\theta_r = 60°$) respectively. Full-wave simulation of the frequency dispersion of propagating scattering amplitudes normalized to that of the incident wave for b) K=8 and d) K=9.

the needed scattering harmonics $(n = 1)$ strongly dominates. It is important that we have minimized the amplitudes not only of propagating spatial harmonics but also those of evanescent harmonics with $|n| \geq 2$. In Fig.2(c), we depict the similar results for K=9 ($\theta_r = 60°$). Once again, the incident plane wave is almost fully reflected in the desired direction. In this particular example, the selected values of the discrete sheet impedance matrix are as follows:

$$Z_{1\text{-}9} = [-85j, -70j, -185j, -185j, -185j, \\ -185j, -102j, -99j, -101j]. \quad (14)$$

In both examples, scattering amplitudes of parasitic spatial harmonics are minimal at 8 GHz, and the needed scattering amplitude approaches unity.

Our next objective is to design the unit cell capable of accommodating the local sheet impedances Z_{1-8} and Z_{1-9} for angles 77° and 60°, and other sheet impedances for other deflection angles in the range $60° - 90°$.

Designing the unitcell: The unit cell that can cover the range of the sheet reactances from -70 to -185 Ohm is formed by a microstrip wire on top of a metal-backed RT5880 substrate which is loaded by a varactor and additional reactance of the effective split-ring resonator The reason behind using a fixed capacitor is provided in the **Appendix. B**. Details of the geometry are shown in the inset of Fig.3(a).

The first gap g_1 of the microstrip wire shown in Fig.3(a) is filled with a hyper-abrupt varactor diode MAVR-000120-14110P. This varactor can operate at frequencies up to 70 GHz, offering low serial resistance and a capacitance range 0.1–1.1 pF [34]. The fixed capacitor which loads the second gap g_2 is GJM1555C1HR15RB12D. This capacitor is chosen due to its fine tolerance ± 0.03 pF. It has the nominal capacitance 0.15 pF [35].

In Fig.3(a), we show the retrieved sheet reactance of the unit cell at 8 GHz plotted versus the varactor capacitance C_v. The sheet impedance turns out to be in the range [-200j, -55j] which completely covers the ranges of Z_{1-8} and Z_{1-9} in two above cases and gives us the freedom to engineer other deflection angles. Besides, in Fig.3(a) one can see the excellent angular stability of the sheet impedance of such unit cell.

In fact, the local reflection coefficient of most reported RISs is unstable with respect to the incidence angle [36]. As vehicles constantly change their positions, the direction of the incoming signal from the automobile UE to the RIS varies over time in an uplink scenario. This means the RIS scattering response must be re-simulated at each time interval, posing a significant challenge. However, as shown in Fig.3(a), the sheet impedance of our designed RIS remains stable regardless of the incident angle. This stability is a crucial factor for seamless vehicular communications, as it eliminates the need for re-simulation to obtain new sheet impedance values when the incident angle changes. This approach is a critical aspect of our optimization framework, as it renders the overall number of RIS elements irrelevant to the computational load. Instead, the number of unit cells within a single supercell determines the number of initial points generated by MultiStart, each of which undergoes local optimization to minimize the cost function effectively. For scenarios requiring the largest deflection angles (where

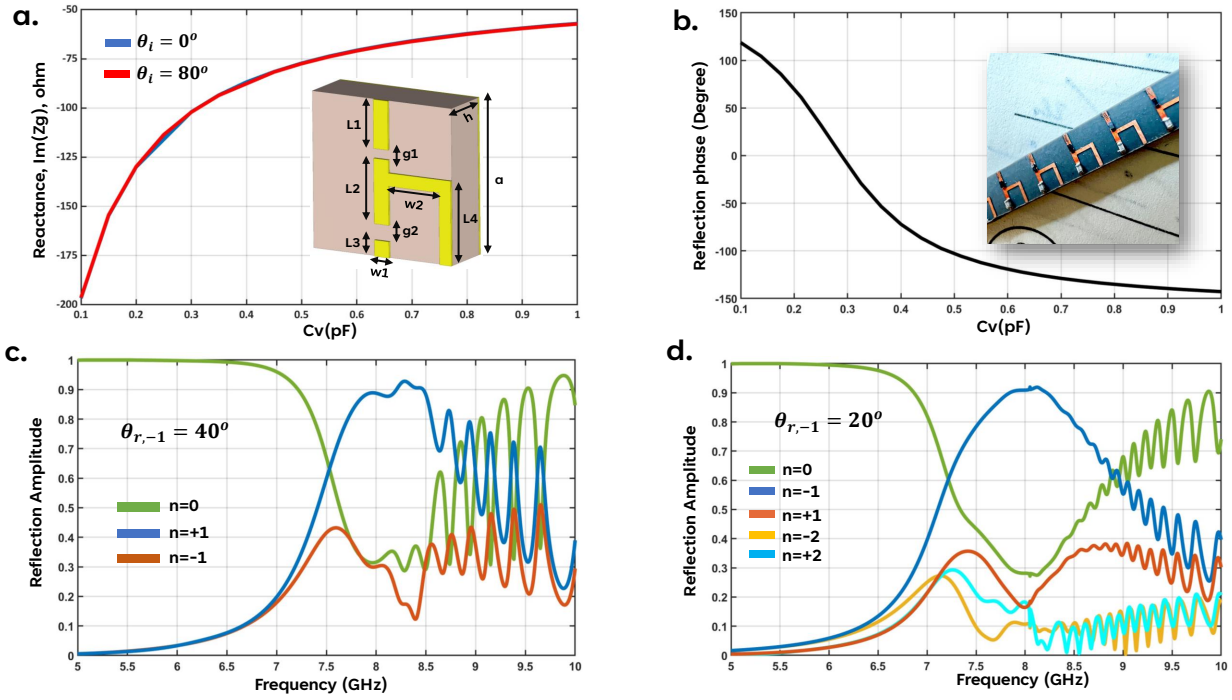

Fig. 3. a) Retrieved value of the sheet impedance against the variations in the varactor capacitance C_v, and the angular stability analysis. The inset of the figure shows the notations of the unit cell geometrical parameters. The dimensions are as follows: [a, h, L1, L2, L4, w2, g1, L3]= [4.8, 1.575, 1.5, 2, 2.6, 2.15, 0.3, 0.5] mm, w1=g2=L3. b) Local reflection phase of the uniform metasurface ("θ_i") versus the varactor capacitance C_v. c) Frequency dispersion of the reflection amplitude of an infinite periodically non-uniform RIS with our original geometry whose biasing voltage distribution is found by the phase-gradient method. Full-wave simulations for $\theta r = 40°$. d) The same amplitude for $\theta r = 20°$ when the biasing voltage distribution is obtained by the method of slowly-varying phase.

the supercell has the smallest number of unit cells, K=6), the total optimization time was approximately 40 seconds on our workstation (Z3 Tower G9 with an Intel Core i5 processor and 96 GB of RAM). For smaller deflection angles (with a supercell containing up to K=25), the optimization time increased to roughly 2 minutes.

Full-Wave Numerical Validation: The next step is to implement the optimal discrete sheet impedance profile presented in Figs.2(a) and (c) with the actual unitcell. Following the values presented in Fig.3(a), the required varactor capacitances C_v can be obtained equating the values Z_{1-8} and Z_{1-9} to $1/j2\pi FC_v$, where $F = 8 \cdot 10^9$ Hz. Fig.2(b) and (d) show the reflection amplitude of the infinite periodic RIS with K=8 ($\theta_r = 77°$) and K=9 ($\theta_r = 60°$) respectively. Based on Eq. 3, there are three propagating Floquet-Bloch harmonics (open channels) at our working frequency. The lines represents the scattering coefficient for the desired harmonic (n=+1) assuming all the varactors are lossless, that gives the reflection amplitude 0.99. As a result, the power efficiency η, calculated for the n-th mode of our periodic RIS as the square power of the modal reflection coefficient $\eta = |\Gamma_n|^2$, is nearly equals 0.98 for n=+1. In other words, full-wave numerical simulations agree very well with our theory and confirm that the incident plane wave is almost fully reflected in the needed direction. Indeed, when we take into account the losses in the varactors and capacitors, the efficiency will decrease as we will see in the next section. Another harmful factor for the efficiency is the finite size of the RIS that implies additional scattering losses. However, these preliminary calculations clearly show that our method is advantageous for scattering efficiency.

C. Deflection below $\sim 60°$

Next, we show that the diagonal approach (the phase-gradient RIS engineered using the locally periodic approximation) is sufficient to achieve highly efficient anomalous reflection for $\theta_r < 60°$. In this approximation, the local reflection phase of the normally incident wave is equated to that of an infinite array of identical unit cells. Previous research [8] has already established that linear phase gradient metasurfaces offers high-efficient anomalous reflection for $\theta_i < 60°$, and the nearly perfect retroreflection. Fig.3(b) shows the local reflection phase of the uniform MS ("θ_i" in the diagonal matrix representation) versus the varactor capacitance. Varying C_v within the practical range 0.1-1 pF, the maximally achievable difference of the θ_i would be $\Delta\theta_{Cv=0.1-1}$ is near $270°$. This phase coverage is sufficient for practical applications and can still provide satisfactory performance in many scenarios [37], [38]. Note that β_i (local reflection amplitude) is near unity for the lossless scenario.

Full-Wave Numerical Validation: In our first study of the deflection below $60°$, we put $\theta_i = 0°$ and $\theta_r = 40°$. In this case, we have $D = 1.55\lambda$, and every period consists of K =12 unit cells. According to Eq. 3, the system allows for three open Floquet-Bloch channels (propagating harmonics) at 8 GHz. In Fig.3(c), the reflected amplitude of propagating harmonics is

plotted versus frequency for the lossless scenario. Observing the plot, we find that the maximum amplitude of the desired harmonic (n=+1) occurs at 8.3 GHz (slightly different from the target frequency). This error is due to the discrete nature of our reflector. The smallness of the error demonstrates the success of the design based on the local periodic approximation when $\theta_r = 40°$, with an efficiency of $\eta_{K=12}$ = 93% at 8.3 GHz and 88% at 8 GHz. The absolute maximum $\eta = 0.93$ is very close to the fundamental limit for the efficiency of phase-gradient reflectors (see Eq. (15) of [39]).

The second study is done for $\theta_i = 0°$ and $\theta_r = 20°$. This scenario represents a typical example involving a small deviation angle where the surface impedance of the MS slowly linearly varies along the trace of the wave incidence plane. In this case, the RIS should exhibit the periodicity of $D = 2.9\lambda$, and each supercell consists of K =23 elements, whereas C_v varying within the range 0.1-1 pF, encompasses the same maximal local phase difference $\Delta\theta_{Cv=0.1-1}$ = 270° as in the previous case. Fig. 3(d) presents the dispersion of the reflection amplitude of propagating harmonics. Notably, this configuration generates five open channels. The power flux is reflected in the desired direction (n=+1) with the efficiency $\eta_{K=23}$ = 83%. Again, the absolute maximum of efficiency occurs at a frequency, slightly deviating from the operational one (8.2 GHz).

Both these examples illustrate the fact that the RIS designed in accordance with the reflection locality approximation (diagonal matrix method), scatters into many directions that restricts the efficiency. In contrast, our surface impedance method, as it is discussed in Section II, grants the suppression of unwanted spatial harmonics and keeps maximally efficient reflection toward the UE even for large deflection angles. Improved signal quality and coverage, seamless connectivity without the need for re-simulation of RIS fundamental parameters, and versatility and adaptability make our approach highly effective for dynamic environments. Also, the bandwidth of our proposed RIS system is in the range of few hundreds of MHz, which is sufficient for a wide range of wireless communication applications.

IV. Experimental validation

A. Measurement setup

In this section, we propose our novel biasing approach for testing reconfigurable surfaces inside the parallel-plate waveguide (PPW). This method offers significant advantages in terms of cost-effectiveness, making it highly beneficial for practical applications when the RIS is uniform along one axis. A key aspect of this method is that it requires only one row of the RIS, rather than the entire surface. This significantly decreases the amount of required materials, particularly costly varactors, by nearly 1/50. This reduction in materials translates directly to lower production and testing costs, making it more feasible to conduct multiple tests and iterations without incurring high expenses. Additionally, the PPW setup allows for precise control over experimental variables such as the angle of incidence, frequency, and biasing voltages. This precision reduces the likelihood of errors and the need for re-tests, ensuring that the results are accurate and dependable.

Based on image theory, 1D array of the RIS mimicking the infinite number of unitcells in the y-direction while it comprised 45 unit cells in the x-direction (See the fabricated sample in the inset of Fig. 3(b)). By adjusting the bias voltage of each varactor, we achieved the impedance matrices $Z_{1...K}$, for each reflection angle θ_r. Fig.4(a) shows the bottom plate of our waveguide. It is a copper plate of size 1×2 m with the arrayed perforation on the circle of radius 0.49 m dedicated for the insertion of the receiving probe. These holes have the 3 mm diameter and do not have a practical impact on the field distribution. The region 1 is for the main measurement and it is separated from the region 2 which is dedicated for the ground plane measurement to normalize the results. The transmitting probe (of fixed location Feed 1) excites the quasi-TEM wave in the waveguide, and the circular array holes allows us to measure the complex transmission coefficient S_{21} as a function of the scattering angle θ with the step 3° using a vector network analyzer.

To ensure the parallelism of the copper plates, we utilized holders of the same thickness as the unit cell size ($P = 4.8$ mm). In the inset of Fig.4(b), the space between the two copper plates is shown (magnified in the inset). The holders were coated with TG-FAM6 absorbers to prevent the distortion of the electromagnetic field. The same holders were also located in the region 2 that was necessary for the set of normalization measurements (which is not shown in the figure).

The normalization measurements (region 2) are necessary so that to properly assess the power scattered by our array. In this set of measurements, we excited the waveguide in the region 2 (by Feed 2) and the wave illuminated the back ground plate of the array ($S_{21}^{(0)}(\theta)$). This scattering pattern allows us to properly measure the scattering efficiency of the RIS normalizing $S_{21}(\theta)$ to $S_{21}^{(0)}(\theta)$, i.e. $\eta(\theta) = |S_{21}(\theta)/S_{21}^{(0)}(\theta)|^2$. Since the flat strip utilized for normalization was the ground plane of our array, the same holders and absorbers should have been placed in both regions 1 and 2 making these regions electromagnetically identical.

To implement the biasing, we made the cutaway of size 100×21.6 cm in the top copper plate, as shown in Fig.4(b). Into this cut, we inserted a PCB with 45 parallel strips on its bottom surface, separated from each other by tiny gaps. The top surface of this PCB was covered by a copper sheet so that to esnure the electromagnetic integrity of our waveguide. The sheet impedance of the array of biasing strips is very small, and the distance 0.5 mm between this array and the copper sheet (equal to the thickness of the PCB) is deeply subwavelength. As a result, the surface impedance of the biasing array is close to 0 as well as that of polished copper. Therefore, the biasing sample shown in Fig.4(c) does not disturb the operation of our parallel-plate waveguide. The wires of every unit cell were soldered to the biasing strips. Fig.4(d) shows the other side of the biasing array whose strips are individually connected to the so-called Jumper cables. Subsequently, the needed biasing voltages were applied to every varactor separately. To simplify the circuit distributing the voltages between the biasing strips, we used four DC voltage supplies. The negative poles of every varactor (located at the bottom of every unit cell) were soldered to the lower

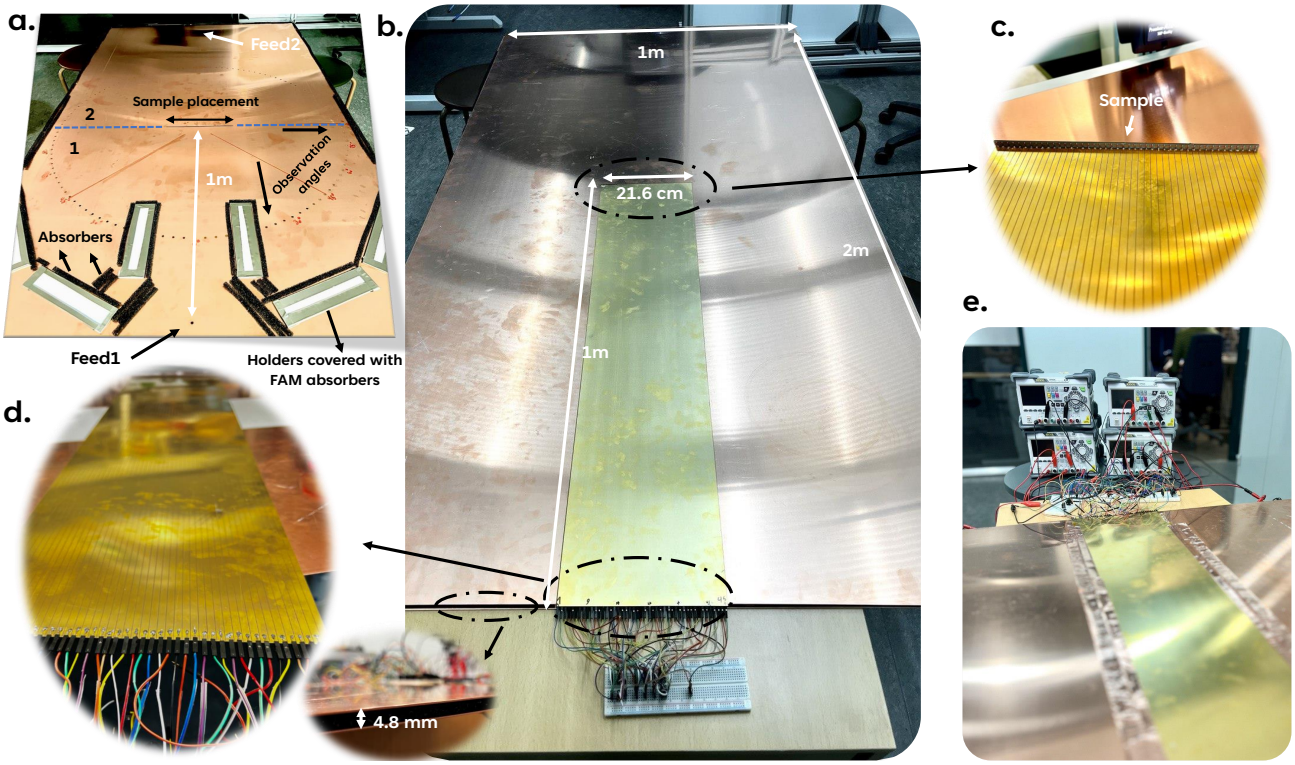

Fig. 4. a) The lower plate of the horizontal parallel plate waveguide with the holes drilled for inserting the receiving probe (S-parameters measurement). The holders covered with absorbing sheets are used to support the upper plate. b) The general picture of the whole setup with the inset showing the gap between the plates. c) The sample soldered to the strips of the printed circuit board (PCB). d) The Jumper wires connected to the other side of the PCB. e) The DC voltage supply connected to the wires so that to separately bias every varactor.

copper plate of our waveguide.

As it was already noticed, this novel biasing configuration allows us to separate the DC operation of the setup from the AC (8 GHz) operation. At zero frequency, every varactor is independently adjusted by its DC voltage. At 8 GHz, the microstrip wires of every unit cells are effectively connected to both metal plates of the waveguide.

B. Measurement results

In two critical measurements, we experimentally assess the performance of the RIS at large deflection angles, comparing the biasing scheme of our proposed surface impedance method (section II) against the diagonal matrix phase shift approach (Fig.3(b)). Based on the sheet impedance matrices Z_{1-8} and Z_{1-9} obtained in section III.B (see also in Fig.2), we calculated the necessary varactor capacitances C_v. Then the corresponding reverse DC voltages, were found from the varactor datasheet and applied via the described biasing system. Fig.5(a) and (b) display the efficiency $\eta(\theta)$ we measured for the cases of $\theta_r = 77^\circ$ (Z_{1-8}) and $\theta_r = 60^\circ$ (Z_{1-9}), respectively. In reality, peak efficiencies occurred at $\theta_r = 80^\circ$ (for $K = 8$) and $\theta_r = 66^\circ$ (for $K = 9$). Despite a slight deviation from theoretical predictions, we obtained in both these challenging cases the excellent efficiencies of the anomalous reflection $\eta_{K=8} = 76\%$ and $\eta_{K=9} = 81\%$ which are sufficiently close to those of an infinite lossless MS engineered in the same way. From the curves, it can be seen that the capacitor and varactor losses are approximately 10%, which is within an acceptable range.

So that to demonstrate the advantage of our method, we biased our array using the conventional phase-gradient approach and performed the same measurements [6], [7]. The corresponding results for $\theta r = 77^\circ$ and $\theta r = 60^\circ$, are shown in Fig.5(c) and (d). One may see that our method grants nearly 30% gain in the efficiency compared to the RIS formed by diagonal matrix, that is practically very important taking into account how keen is the issue of energy efficiency in wireless networks. Additionally, in Fig.5(e) we present the experimental results obtained by the phase gradient method (see in Fig.3(c)) for $\theta_r = 40^\circ$. The maximal scattering is observed at $\theta_r = 47^\circ$, whereas $\eta_{K=12} = 58\%$. Indeed, this experimental efficiencies are noticeably lower that those predicted for the infinite MS (see Fig.3). The reason is the excitation of a strong parasitic maximum in the region of negative deflection, that is, of course, absent for the infinite array and is specific namely for this biasing configuration. We assume that this maximum may result from the constructive interference of the so-called edge waves, produced by the ends of our array. The phase quantization, particularly in lower-bit quantized RIS systems, can lead to imaging interference through unintended mirror beams, as shown in prior measurements at 3.5 GHz [40]. In our discrete impedance model, we address this issue by fully canceling and mitigating mirror reflections. However, during experimentation, we observed some undesired reflections, which we attribute to minor inconsistencies in the varactor

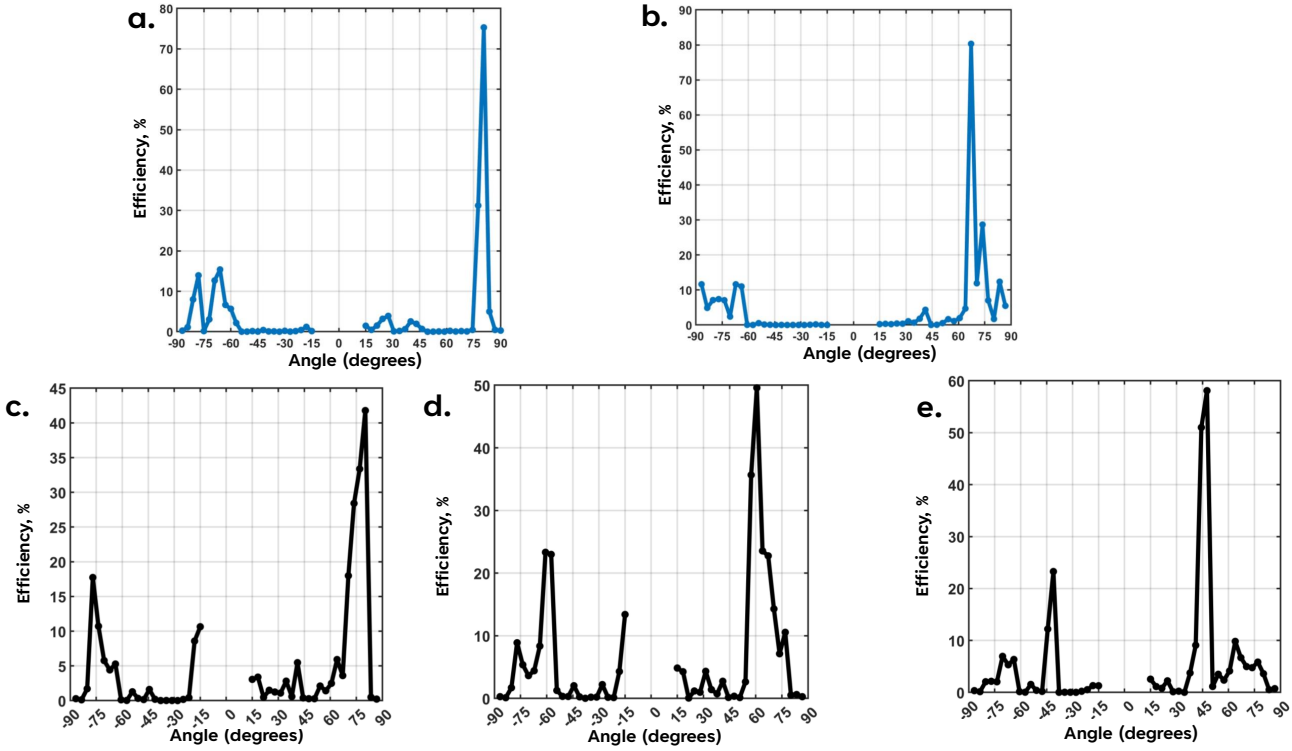

Fig. 5. The measured reflection efficiency corresponding to our optimization method for a) Z_{1-8} ($\theta_r = 77°$), and b) Z_{1-9} ($\theta_r = 60°$) modelled in Section III.B. c), d) and e) are the reflection efficiencies measured in the cases when the biasing voltage was distributed in accordance to the conventional diagonal matrix approach. c) is for $\theta_r = 77°$, d) is for $\theta_r = 60°$, and e) is for $\theta_r = 40°$.

diodes' capacitance relative to datasheet specifications.

C. Role of Fixed Capacitor in the Unit Cell

In this Appendix, we will see the role of fixed capacitor in the unitcell. We suggest the original geometry of the unit cell shown in the inset of Fig.1(a). In this geometry, the capacitive grid with sheet impedance Z_s located in the plane $z = 0$ is formed by equidistant microstrip wires loaded by varactors (tunable capacitance C_v) and rectangular microstrip loops which are, in their turn, loaded by lumped capacitors (fixed capacitance C_f). The loop depicted in Fig.1(a) seems open, however, below we will show that it is effectively closed and represents a split-ring resonator operating below its self-resonance. The reactance of the loaded loop X_l is that of the parallel circuit: $X_l = \omega L_l/(1-\omega^2/\omega_0^2)$, where L_l is the loop inductance. At $\omega < \omega_0 = 1/\sqrt{C_f L_l}$ X_l is inductive and this effective inductance is larger than L_l. The series connection of X_l and the reactance of the varactor $X_v = -1/(\omega C_v)$ makes the reactive load per unit length of the microstrip wire nearly resonant. This technical solution drastically enhances the impact of the varactor on the current induced in the microstrip wire.

Due to the presence of the bottom conducting plane the seemingly open loop is equivalent to a closed loop of double vertical size loaded by two fixed capacitors C_f. The incidence of a plane wave to the row of unit cells whose photo is given in Fig.3(b) is modelled by the incidence of the quasi-TEM mode of a parallel-plate waveguide excited by a vertical monopole. So, the row of unit cells shown Fig.3(a) and Fig.5(b) being excited by the mode of a parallel-plate waveguide is practically equivalent to the MS of infinitely long wires having a finite but very large width. In the experiment, the wires are vertically oriented and located between two large horizontal metal plates. The biasing of varactors in each unit cell is possible because every microstrip wire is connected to its own horizontal microstrip connected to the voltage source and electrically separated from the top copper plate (more details of our biasing scheme are given in the experimental section).

V. Outlook

The primary advantage of the discrete impedance model is its capability to increase beamforming efficiency by over 30% compared to conventional diagonal matrix methods, as demonstrated in our prototype experiments. This efficiency boost is particularly valuable in vehicular communication, where signals must dynamically adapt to rapidly changing vehicle positions. Traditional RIS configurations suffer from substantial efficiency loss at higher deflection angles due to parasitic scattering, leading to performance degradation in non-line-of-sight (NLOS) areas. However, our discrete impedance approach minimizes these issues by tailoring the surface impedance profile to maximize beam deflection toward the receiver under dynamic conditions [1].Our discrete impedance model of a metasurface-based RIS has demonstrated superior performance in large-angle deflections, allowing one to redirect beams efficiently even under conditions of frequent spatial shifts, such as when vehicles move at high speeds through urban areas. The model's flexibility in impedance adjustments makes

it especially suitable for vehicle-to-everything (V2X) communication systems, where dynamic reconfigurability is critical to maintaining connectivity.The increased efficiency achieved through our discrete impedance RIS model reduces latency and signal interruptions in high-speed environments by ensuring that beamforming adjustments are responsive to real-time positional changes. This reduction in signal disruption is particularly crucial for safety-critical applications in autonomous driving, where a lapse in connectivity can lead to delayed reaction times in emergency situations [2]. Additionally, the capability of the discrete impedance model to suppress the undesired harmonics minimizes mirror reflections and signal scattering (which introduce noise and latency in conventional RIS configurations). This characteristic makes the model more suitable for vehicle-to-everything (V2X) communication and safety applications, for which minimal latency and high reliability are paramount. Also, idealized unit cell behavior, the impact of fabrication tolerances, measurement noise, finite-size effects, substrate losses, and varactor nonlinearity are challenges that need to be carefully considered when designing for the real-world applications.

VI. Conclusion and Future works

This paper introduces a highly efficient and practical realization of Reconfigurable Intelligent Surfaces (RIS) usefull for different wireless propagation channels particurly vehicular communication. By employing our surface impedance method, we address the inherent limitations of traditional diagonal matrix techniques, especially at large deflection angles. Our investigations in the paper demonstrates that the efficiency of the RIS using the diagonal matrix approach is at least 30% lower than our proposed optimizaing method. This enhancement is crucial for vehicular environments where maintaining robust and reliable connectivity is essential due to the high mobility and dynamic nature of vehicles. We numerically and exprimentaly validated the required optimum surface/sheet impedance which was obtained through our inverse optimization framework in Matlab.

Our proposed optimization approach focuses on individual supercells rather than the entire surface, resulting in a significantly faster optimization process. The varactor used in our design can switch in the nanosecond range, and for industrial applications, an FPGA can be configured to control the network's biasing within milliseconds. This makes our RIS particularly suitable for highly dynamic environments such as vehicular communications. Additionally, the angular stability of the sheet impedances against incident angles eliminates the need for re-simulation of RIS surface impedance. This ensures seamless communication and ubiquitous connectivity, enhancing the quality of service by boosting the received signal.

For experimental validation, using the parallel plate waveguide was a wisely choice, as it requires only a single row of the RIS rather than the entire surface. This approach offers several advantages: reduced material costs, simplified fabrication, lower infrastructure requirements, and improved repeatability and reliability. By adjusting the biasing voltage of the varactor diodes, we effectively steer the scattered beam into different angles and measure the efficiency in the far-field. This setup allowed us to compare our optimized method with the diagonal matrix phase shift approach simply by changing the network bias. The comparison demonstrated a significant enhancement in the RIS reradiation efficiency using our method.

Note that our presented method is restricted to periodical RIS configurations. For aperiodic RIS, a global optimization of all unit cells is required for each scenario of anomalous reflection, leading to significantly longer computation times for the RIS processor. Additionally, our current work is limited to single polarization, as it generates different surface impedance values for different polarizations. To extend this approach to dual polarization applications (polarization-division multiplexing), different unitcell design should be considered. This can be a promising area for future research.

Acknowledgment

The authors acknowledge the use of facilities of Aalto University at Microwave Laboratory. They would like to thank Antti Kuhlberg and Matti Vaaja for their great support during the setup fabrication and measurements.

Appendix

A. Optimization Framework

1) Input Parameters & Initialization: The optimization framework begins by defining the key parameters required for solving the inverse problem of determining the RIS sheet impedance.

2) Define Input Parameters:

- **Frequency** (f) – The operational frequency of the RIS.
- **Deflection Angle** (θ_d) – The desired beam steering direction.
- **Substrate Properties**:
  - Relative permittivity (ε_r).
  - Thickness (h).
  - Loss tangent ($\tan\delta$).
- **Number of Unit Cells in the Supercell** (K) – The number of elements in each periodic supercell.
- **Fourier Transform Components** – Used to compute the impedance profile.

3) Initialize Optimization Environment:

- Set up **reproducibility** by using `rng default` (to ensure consistent results).
- Enable **parallel processing** to speed up the computation.
- Use **MultiStart Optimization** to efficiently search for optimal impedance values.

4) Define Initial Points:

- The optimization requires multiple starting points for the variables $x_1, x_2, ..., x_K$, which correspond to the impedance values of each unit cell.
- These initial points are **randomly generated** and combined into a matrix using `combvec`, a function that creates all possible combinations of input vectors.

5) Define the Optimization Problem:

6) Define Objective Function: The goal is to **minimize** the difference between the actual reflected amplitude A_{calc} and the desired reflected amplitude A_{goal}. The objective function is formulated as:

$$F(Z_1, ..., Z_K) = |A_{\text{calc}} - A_{\text{goal}}| \tag{15}$$

7) Define Constraints:

- **Variable Bounds** – Impedance values must be **within the achievable range of the varactor diodes** ($-300j$ to $-50j$).
- **Linear & Nonlinear Constraints**:
  - Ensure that the impedance profile follows physical constraints.
  - Prevent solutions that lead to undesired scattering.

8) Run the Optimization Algorithm:

- **Execute MultiStart Optimization**: This method runs multiple instances of the optimization problem from different starting points, avoiding local minima.
- `Fmincon` is used as the solver for constrained nonlinear optimization.

9) Compute Impedance and Admittance Matrices: After optimization, the impedance and admittance matrices are computed to model the behavior of the RIS.

10) Compute Free-Space Impedance Matrix Z_0: The matrix Z_0 is initialized as a **Toeplitz matrix**, representing the free-space impedance of different Floquet harmonics. The diagonal elements are calculated as:

$$Z_0(n, n) = \frac{\mu_0 \omega_0}{k_{x,n}} \tag{16}$$

where $k_{x,n}$ is the wave number component of the reflected Floquet harmonics.

11) Compute Grounded Dielectric Substrate Impedance Matrix Y_d: The substrate impedance is calculated using:

$$Z_d(n, n) = \frac{\mu_0 \omega_0}{k_{d,x,n} \tanh(\gamma_n d)} \tag{17}$$

where γ_n is the propagation constant in the dielectric.

The admittance matrix Y_d is then derived from Z_d.

12) Solve for Optimal Reflection Coefficients: Using the computed matrices, the optimization framework determines the reflection coefficients which is defined in Eq. 11 and Eq. 12.

13) Reconstruct the Optimal Impedance Profile: The optimized **Fourier coefficients** of the impedance profile are used to reconstruct the admittance function as defined in Eq. 2.

The admittance profile is then **converted back into impedance values** for practical implementation.

14) Apply the Optimized Impedance to the RIS:

- The final step applies the computed impedance values to the **physical RIS unit cells**.
- The optimized values are used to adjust the **varactor diode capacitances**, which are then implemented in the **experimental prototype**.

15) Key Features of the Optimization Framework:

- **Inverse Design for Maximum Efficiency** – Ensures that the RIS **reflects energy in the desired direction** with minimal loss.
- **Toeplitz Matrix Representation** – Enables **fast computation** using the Fourier transform.
- **MultiStart Optimization** – Prevents local minima issues, ensuring **global optimization**.
- **Scalable for Large RIS Arrays** – The optimization focuses on **individual supercells**, making it computationally feasible.
- **Suppresses Unwanted Harmonics** – Eliminates mirror reflections and parasitic scattering for **clearer signal transmission**.

The step by step framework is also listed below.

Algorithm 1 Inverse optimization for obtaining RIS sheet impedance

Input: Frequency, Deflection angle θ_d, Substrate parameters (ε_r, and $\tan\delta$)
Output: Optimized sheet impedance values, Z_{1-K}
Initialize and set up optimization environment:
    Set reproducibility with **rng default**
    Initialize MultiStart with parallel processing
Step 1: Define Initial Points
Specify the number of initial points for each variable $x_1, x_2, \ldots, x_K$
Combine initial points into a matrix using **combvec**
Step 2: Define Optimization Problem
Define the objective function **fun**
Call Algorithm 2, This objective function should be minimized
Set variable bounds, linear constraints, and nonlinear constraints using *@nlcons*
Step 3: Run Optimization
Execute MultiStart optimization
Step 4: Calculate Impedance and Admittance Matrices
Call Algorithm 3 to compute impedance and admittance matrices
Step 5: Reconstruct Admittance Profile
Reduce the Fourier coefficients array
Construct the admittance profile using Fourier components

Algorithm 2 Objective Function for Optimization

procedure OBJECTIVEFUNCTION(x)
  Calculate Loss Tangent: LossTan $\leftarrow 0.0002$
  Calculate substrate permittivity and thickness ϵ_r, h
  Define frequency and basic parameters
  Compute impedance values z_1 to z_K
  Construct admittance profile ys
  Perform Fourier Transform on ys to get yp
  Build admittance matrix Ys from yp
  Compute reflection coefficient matrix Γ
  Calculate reflection coefficients R
  Calculate Objective Value:
  $z \leftarrow \text{abs}(R(N+1)-0) + \text{abs}(R(N-1) - 1/\sqrt{\cos\theta_i/\cos\theta_r}) + \text{abs}(R(N)-0)$
  $z \leftarrow z + \text{abs}(\sum(R(N+3:2N+1)) - 0)$
end procedure

Algorithm 3 Compute Impedance and Admittance Matrices

procedure COMPUTEIMPEDANCEADMITTANCE(N, k_0z, k_0n, w_0, mue_0, $beta_m$, d)
  Initialize matrix $Z0$ to zeros of size $(2N+1)\times(2N+1)$
  Initialize matrix Yd to zeros of size $(2N+1)\times(2N+1)$
  for $rr = 1$ to $2N+1$ **do**
    for $cc = 1$ to $2N+1$ **do**
      $k_{0zn} \leftarrow k_0z + (cc - N - 1)\cdot beta_m$
      if $|k_{0zn}| \le |k_0n|$ **then**
        $k_{0xn} \leftarrow \sqrt{k_0n^2 - k_{0zn}^2}$
      else
        $k_{0xn} \leftarrow -\sqrt{k_0n^2 - k_{0zn}^2}$
      end if
      if $cc == rr$ **then**
        $Z0[rr, cc] \leftarrow \frac{mue_0\cdot w_0}{k_{0xn}}$
      end if
    end for
  end for
  for $rr = 1$ to $2N+1$ **do**
    for $cc = 1$ to $2N+1$ **do**
      $k_{dzn} \leftarrow k_0z + (cc - N - 1)\cdot beta_m$
      if $|k_{dzn}| \le |k_dn|$ **then**
        $k_{dxn} \leftarrow \sqrt{k_dn^2 - k_{dzn}^2}$
      else
        $k_{dxn} \leftarrow -\sqrt{k_dn^2 - k_{dzn}^2}$
      end if
      $\gamma_n \leftarrow 1i\cdot k_{dxn}$
      $Zd_n \leftarrow \frac{mue_0\cdot w_0}{k_{dxn}}$
      if $cc == rr$ **then**
        $Yd[rr, cc] \leftarrow \frac{1}{Zd_n\cdot\tanh(\gamma_n\cdot d)}$
      end if
    end for
  end for
end procedure

VII. CONTRIBUTIONS

Dr. X. Wang and Dr. S. Kosulnikov previously worked on the project to enhance the efficiency of anomalous reflection for static MS, contributing by developing the optimization framework in MATLAB. Building on their work, the author extended this concept to practical reconfigurable RIS. The author conducted the numerical simulations, designed the unit cell, and prepared the manuscript draft. Additionally, the author ordered the proto- type, set up the measurement system, and carried out the measurements. Prof. C. Simovski edited the draft and supervised the project.

REFERENCES

[1] A. V. Jha, B. Appasani, M. S. Khan, S. Zeadally, and I. Katib, "6g for intelligent transportation systems: standards, technologies, and challenges," *Telecommunication Systems*, pp. 1–28, 2024.

[2] M. Di Renzo, A. Zappone, M. Debbah, M.-S. Alouini, C. Yuen, J. De Rosny, and S. Tretyakov, "Smart radio environments empowered by reconfigurable intelligent surfaces: How it works, state of research, and the road ahead," *IEEE journal on selected areas in communications*, vol. 38, no. 11, pp. 2450–2525, 2020.

[3] K. Zhu and Y. Zhu, "Evolution of wireless communication technology for v2x assisted autonomous driving," in *Communication, Computation and Perception Technologies for Internet of Vehicles*, pp. 33–59, Springer, 2023.

[4] A. Al-Hilo, M. Samir, M. Elhattab, C. Assi, and S. Sharafeddine, "Reconfigurable intelligent surface enabled vehicular communication: Joint user scheduling and passive beamforming," *IEEE Transactions on Vehicular Technology*, vol. 71, no. 3, pp. 2333–2345, 2022.

[5] Z. Ji, P. L. Yeoh, D. Zhang, G. Chen, Y. Zhang, Z. He, H. Yin, *et al.*, "Secret key generation for intelligent reflecting surface assisted wireless communication networks," *IEEE Transactions on Vehicular Technology*, vol. 70, no. 1, pp. 1030–1034, 2020.

[6] F. Liu, D.-H. Kwon, and S. Tretyakov, "Reflectarrays and metasurface reflectors as diffraction gratings: A tutorial.," *IEEE Antennas and Propagation Magazine*, 2023.

[7] Q. Wu and R. Zhang, "Intelligent reflecting surface enhanced wireless network via joint active and passive beamforming," *IEEE Transactions on Wireless Communications*, vol. 18, no. 11, pp. 5394–5409, 2019.

[8] A. Díaz-Rubio and S. A. Tretyakov, "Macroscopic modeling of anomalously reflecting metasurfaces: Angular response and far-field scattering," *IEEE Transactions on Antennas and Propagation*, vol. 69, no. 10, pp. 6560–6571, 2021.

[9] N. Yu, P. Genevet, M. A. Kats, F. Aieta, J.-P. Tetienne, F. Capasso, and Z. Gaburro, "Light propagation with phase discontinuities: generalized laws of reflection and refraction," *science*, vol. 334, no. 6054, pp. 333–337, 2011.

[10] J. Shabanpour, V. Lenets, G. Lerosey, S. Tretyakov, and C. Simovski, "Engineering of intelligent reflecting surfaces: Reflection locality and angular stability," *IEEE Transactions on Antennas and Propagation*, 2024.

[11] N. M. Estakhri and A. Alu, "Wave-front transformation with gradient metasurfaces," *Physical Review X*, vol. 6, no. 4, p. 041008, 2016.

[12] A. Epstein and G. V. Eleftheriades, "Synthesis of passive lossless metasurfaces using auxiliary fields for reflectionless beam splitting and perfect reflection," *Physical review letters*, vol. 117, no. 25, p. 256103, 2016.

[13] A. Díaz-Rubio, V. S. Asadchy, A. Elsakka, and S. A. Tretyakov, "From the generalized reflection law to the realization of perfect anomalous reflectors," *Science advances*, vol. 3, no. 8, p. e1602714, 2017.

[14] T. He, T. Liu, S. Xiao, Z. Wei, Z. Wang, L. Zhou, and X. Cheng, "Perfect anomalous reflectors at optical frequencies," *Science advances*, vol. 8, no. 9, p. eabk3381, 2022.

[15] Y. Ra'di and A. Alù, "Reconfigurable metagratings," *Acs Photonics*, vol. 5, no. 5, pp. 1779–1785, 2018.

[16] X. Wang, A. Díaz-Rubio, and S. A. Tretyakov, "Independent control of multiple channels in metasurface devices," *Physical Review Applied*, vol. 14, no. 2, p. 024089, 2020.

[17] V. S. Asadchy, M. Albooyeh, S. N. Tcvetkova, A. Díaz-Rubio, Y. Ra'di, and S. Tretyakov, "Perfect control of reflection and refraction using spatially dispersive metasurfaces," *Physical Review B*, vol. 94, no. 7, p. 075142, 2016.

[18] D.-H. Kwon, "Lossless scalar metasurfaces for anomalous reflection based on efficient surface field optimization," *IEEE Antennas and Wireless Propagation Letters*, vol. 17, no. 7, pp. 1149–1152, 2018.

[19] A. Díaz-Rubio, J. Li, C. Shen, S. A. Cummer, and S. A. Tretyakov, "Power flow–conformal metamirrors for engineering wave reflections," *Science advances*, vol. 5, no. 2, p. eaau7288, 2019.

[20] S. Kosulnikov, X. Wang, and S. A. Tretyakov, "Discrete-impedance metasurfaces for wireless communications in d-band," *IEEE Transactions on Antennas and Propagation*, 2023.

[21] S. Shen, B. Clerckx, and R. Murch, "Modeling and architecture design of reconfigurable intelligent surfaces using scattering parameter network analysis," *IEEE Transactions on Wireless Communications*, vol. 21, no. 2, pp. 1229–1243, 2021.

[22] H. Li, S. Shen, and B. Clerckx, "Beyond diagonal reconfigurable intelligent surfaces: From transmitting and reflecting modes to single-, group-, and fully-connected architectures," *IEEE Transactions on Wireless Communications*, vol. 22, no. 4, pp. 2311–2324, 2022.

[23] H. Li, S. Shen, M. Nerini, and B. Clerckx, "Reconfigurable intelligent surfaces 2.0: Beyond diagonal phase shift matrices," *IEEE Communications Magazine*, 2023.

[24] M. Nerini, S. Shen, and B. Clerckx, "Discrete-value group and fully connected architectures for beyond diagonal reconfigurable intelligent surfaces," *IEEE Transactions on Vehicular Technology*, 2023.

[25] Q. Li, M. El-Hajjar, and L. Hanzo, "Ergodic spectral efficiency analysis of intelligent omni-surface aided systems suffering from imperfect csi and hardware impairments," *IEEE Transactions on Communications*, 2024.

[26] Q. Li, M. El-Hajjar, Y. Sun, I. Hemadeh, A. Shojaeifard, Y. Liu, and L. Hanzo, "Achievable rate analysis of the star-ris-aided noma uplink in the face of imperfect csi and hardware impairments," *IEEE Transactions on Communications*, vol. 71, no. 10, pp. 6100–6114, 2023.

[27] Q. Li, M. El-Hajjar, I. Hemadeh, D. Jagyasi, A. Shojaeifard, and L. Hanzo, "Performance analysis of active ris-aided systems in the face of imperfect csi and phase shift noise," *IEEE Transactions on Vehicular Technology*, vol. 72, no. 6, pp. 8140–8145, 2023.

[28] Y. Zhao, Y. Feng, A. M. Ismail, Z. Wang, Y. L. Guan, Y. Guo, and C. Yuen, "2-bit ris prototyping enhancing rapid-response space-time wavefront manipulation for wireless communication: Experimental studies," *IEEE Open Journal of the Communications Society*, 2024.

[29] J. An, C. Xu, D. W. K. Ng, G. C. Alexandropoulos, C. Huang, C. Yuen, and L. Hanzo, "Stacked intelligent metasurfaces for efficient holographic mimo communications in 6g," *IEEE Journal on Selected Areas in Communications*, vol. 41, no. 8, pp. 2380–2396, 2023.

[30] X. Jia, J. An, H. Liu, L. Gan, M. Di Renzo, M. Debbah, and C. Yuen, "Stacked intelligent metasurface enabled near-field multiuser beamfocusing in the wave domain," in *2024 IEEE 99th Vehicular Technology Conference (VTC2024-Spring)*, pp. 1–5, IEEE, 2024.

[31] R.-B. Hwang, *Periodic structures: mode-matching approach and applications in electromagnetic engineering*. John Wiley & Sons, 2012.

[32] "3gpp, "7-24 ghz frequency range," tech. rep. (tr) 38.820, 2021, v16.1.0. [online]. available: https://portal.3gpp.org/desktopmodules/ specifications/specificationdetails.aspx?specificationid=3599,"

[33] O. Tsilipakos, F. Liu, A. Pitilakis, A. C. Tasolamprou, D.-H. Kwon, M. S. Mirmoosa, N. V. Kantartzis, E. N. Economou, M. Kafesaki, C. M. Soukoulis, *et al.*, "Tunable perfect anomalous reflection in metasurfaces with capacitive lumped elements," in *2018 12th International Congress on Artificial Materials for Novel Wave Phenomena (Metamaterials)*, pp. 392–394, IEEE, 2018.

[34] "Mavr-000120-1411 datasheet. accessed: May. 2021. [online]. available: https://cdn.macom.com/datasheets/mavr-000120-1411.pdf.,"

[35] "https://search.murata.co.jp/ceramy/image/img/a01x/g101 /eng/gjm1555c1hr15rb12-01a.pdf,"

[36] J. Shabanpour and C. R. Simovski, "Angular and polarization stability of broadband reconfigurable intelligent surfaces of binary type," *IEEE Access*, vol. 10, pp. 126253–126268, 2022.

[37] Z. Chen, H. Deng, Q. Xiong, and C. Liu, "Phase gradient metasurface with broadband anomalous reflection based on cross-shaped units," *Applied Physics A*, vol. 124, pp. 1–8, 2018.

[38] J. Zhang, L. Yang, L. Li, T. Zhang, H. Li, Q. Wang, Y. Hao, M. Lei, and K. Bi, "High-efficiency polarization conversion phase gradient metasurface for wideband anomalous reflection," *Journal of Applied Physics*, vol. 122, no. 1, 2017.

[39] Y. Li, X. Ma, X. Wang, G. Ptitcyn, M. Movahediqomi, and S. A. Tretyakov, "All-angle scanning perfect anomalous reflection by using passive aperiodic gratings," *IEEE Transactions on Antennas and Propagation*, 2023.

[40] S. Zhang, H. Sun, R. Yu, H. Cui, J. Ren, F. Gao, S. Jin, H. Xie, and H. Wang, "Ris-aided communications at 3.5 ghz: Some insights from practical measurement results," in *2023 IEEE/CIC International Conference on Communications in China (ICCC)*, pp. 1–6, IEEE, 2023.